Efficient spectral and pseudospectral algorithms for 3D simulations of waves in plasmas

Nail A. Gumerov*, Alexey V. Karavaev†, A. Surjalal Sharma‡, Xi Shao§,
and Konstantinos D. Papadopoulos¶
University of Maryland, College Park, MD 20742.

January 20, 2010

Abstract

Efficient spectral and pseudospectral algorithms for simulation of linear and nonlinear 3D whistler waves in a cold electron plasma are developed. These algorithms are applied to the simulation of whistler waves generated by loop antennas and spheromak-like stationary waves of considerable amplitude. The algorithms are linearly stable and show good stability properties for computations of nonlinear waves over tens of thousands of time steps. Additional speedups by factors of 10-20 are achieved by using graphic processors (GPUs), which enable efficient numerical simulation of the wave propagation on relatively high resolution meshes (tens of millions nodes) in personal computing environment. Comparisons of the numerical results with analytical solutions and experiments show good agreement. The limitations of the codes and the performance of the GPU computing are discussed.

Key words: whistler waves, waves in plasma, pseudospectral methods, graphic processors.

1 Introduction

Waves in plasmas in nature and laboratory are generated over a wide range of frequencies. In nature, whistlers, which are first reported in 1919 by Barkhausen [1], are audio-frequency electromagnetic perturbations generated by lightning flashes. These are circularly polarized waves in plasma carried by electrons in the range below the electron cyclotron frequency and above the lower hybrid frequency [2], [3]. Such waves can be generated under many conditions, e.g., by antennas, and space and laboratory experiments can be carried out. Recent laboratory experimental studies of these waves generated by rotating magnetic field sources are conducted at Large Plasma Device (LAPD) located at UCLA [4], [5]. The major interest here is to understand spatio-temporal structures of the waves as a function of the plasma and the magnetic field source parameters.

Using the fluid model of plasmas, the whistler waves can be thought as waves in a medium with strong anisotropic dispersion, considerable nonlinearity, and small dissipation. Usually these waves are substantially three dimensional and in general 3D settings their properties and parametric dependences have not been studied in depth. There is a strong need in efficient numerical methods and implementations as tools for such studies. An approach for a simple and accurate numerical algorithm for whistler computations was suggested in [6] as a part of HEMPIC (hybrid electromagnetic PIC) code. In Cartesian coordinates and periodic boundary conditions this algorithm turns into a pseudospectral method based on the FFT where at each time step an elliptic equation has to be solved in the k-space, while time propagation is handled by an explicit method (using an original predictor-corrector-corrector scheme with improved stability properties). The cited algorithm was tested and showed a good performance for computation of 2D problems (we also

*gumerov@umiacs.umd.edu (corresponding author)
†a.v.karavaev@gmail.com
‡ssh@astro.umd.edu
§xshcn@astro.umd.edu
¶dpapadop@umd.edu

implemented this algorithm in 1D, 2D, and 3D as is and made our own tests). However to run 3D cases on reasonable grids this algorithm becomes rather slow, plus it requires substantial memory. 2D pseudospectral computations of nonlinear whistler waves were also performed in [7] and 3D spheromaks in [8].

The major goal of this paper is to present an optimized algorithm, which we called Whistnl, which is faster and uses less memory. Moreover, as any FFT-based pseudospectral method the algorithm can be relatively easily parallelized. Recent advances in programming and scientific computing using graphic processors (GPU) enable additional acceleration. In this paper we present a new code with algorithmic improvements and discuss the use of the GPU which allows one to run cases on substantial spatial grids (e.g. 256×256×512) in personal computing environment for a reasonable time. The computational time per step was reduced two orders of magnitude for the same accuracy by these means. We also studied linearized equations, which in many cases are appropriate for modeling of whistlers. In this case an analytic solution of the problem is available in the k-space, which can be used to obtain solution at any time without marching in time. These results are consistent with 2D linear theory was applied to compute propagation of whistler wave packets [9]. Some issues of modeling of whistler excitation by thin antennas, supported by computations and comparisons with experiments, are discussed as well. We also present a new solution for spheromak-like stationary waves of an arbitrary amplitude, which has been tested numerically using the methods for whistler waves.

2 Model

2.1 Basic equations

The mathematical model used in the present paper for simulation of the whistler waves consists of the electron fluid and Maxwell's equations, and is similar to [6]. The model assumes that the displacement current can be neglected, the ions are stationary, and the plasma is cold electron fluid.

In this case the Faraday's and Ampere's laws plus equation for electron motion can be written in the form

$$\nabla \times \mathbf{E} = -\frac{1}{c}\frac{\partial \mathbf{B}}{\partial t}, \tag{1}$$

$$\nabla \times \mathbf{B} = -\frac{4\pi}{c} e n_e \mathbf{v}_e, \tag{2}$$

$$\frac{\partial \mathbf{v}_e}{\partial t} + (\mathbf{v}_e \cdot \nabla)\,\mathbf{v}_e = -\frac{e}{m_e}\mathbf{E} - \frac{e}{m_e c}\mathbf{v}_e \times \mathbf{B} - \nu_e \mathbf{v}_e, \tag{3}$$

where $\mathbf{E}$ and $\mathbf{B}$ are the electric and magnetic fields, $\mathbf{v}_e$ and n_e are the electron velocity and the number density, respectively, e and m_e are the electron charge and mass, c is the speed of light in vacuum and ν_e is the collision frequency. We note that the first equation shows that the divergence of $\mathbf{B}$ does not change in time. So if this field had zero divergence at $t = 0$ then

$$\nabla \cdot \mathbf{B} = 0 \tag{4}$$

for any $t > 0$. Also we note there are no sources of electrons. This means that in the number density equation

$$\frac{\partial n_e}{\partial t} + \nabla \cdot (n_e \mathbf{v}_e) = 0, \tag{5}$$

the divergence term is zero due to Eq. (2) and n_e does not change in time. So if $n_e = n_0 = const$ is uniform at $t = 0$, then the same will hold for any $t > 0$. Eqs (1)-(3) here define the electron-magnetohydrodynamic (EMHD) model [10].

Eqs (1)-(3) can be written in dimensionless form using typical scales. These scales are determined by the electron plasma frequency $\omega_{pe} = \left(4\pi n_0 e^2/m_e\right)^{1/2}$ and the electron cyclotron frequency $\Omega_e = eB_*/(m_e c)$ for magnetic field of magnitude B_*, which introduces the scale for $\mathbf{B}$. These frequencies introduce the length

and time scales $\lambda_e = c/\omega_{pe}$ and $t_e = 1/\Omega_e$, where the first one is the electron skin depth. Based on this the following dimensionless variables can be defined

$$\overline{t} = \frac{t}{t_e} = \Omega_e t, \quad \overline{\mathbf{x}} = \frac{\mathbf{x}}{\lambda_e}, \tag{6}$$
$$\overline{\mathbf{v}} = \frac{t_e}{\lambda_e}\mathbf{v}_e, \quad \overline{\mathbf{B}} = \frac{1}{B_*}\mathbf{B}, \quad \overline{\mathbf{E}} = \frac{ct_e}{\lambda_e B_*}\mathbf{E},$$

and dissipation parameter $\overline{\nu} = \nu_e/\Omega_e$, which is the only parameter entering the dimensionless equations

$$\nabla \times \mathbf{E} = -\frac{\partial \mathbf{B}}{\partial t}, \tag{7}$$
$$\nabla \times \mathbf{B} = -\mathbf{v},$$
$$\frac{\partial \mathbf{v}}{\partial t} + (\mathbf{v}\cdot\nabla)\,\mathbf{v} = -\mathbf{E} - \mathbf{v}\times\mathbf{B} - \nu\mathbf{v}.$$

In these equations the bars over dimensionless variables have been dropped for simplicity.

3 Modeling of waves generated by antenna current

To solve the system of governing equations initial and boundary conditions should be provided. However, if a numerical solution should be obtained on a grid while the waves are driven by thin (wire-type) antennas, high resolutions should be provided in the vicinity of the wires to satisfy the boundary conditions. In fact, it is not difficult to modify system (7) to include the effect of wires with prescribed currents and avoid boundary conditions on the wires. In these equations the magnetic field $\mathbf{B}$ consists of the background field $\mathbf{B}_0$ of zero curl, and the field generated by motion of cold fluid with source $-\mathbf{v}$. This source term is zero inside the wires. On the other hand the source term corresponding to the antenna current, $\mathbf{j}_{ant}$, is localized inside the wire. Therefore, total magnetic field in the domain both inside and outside the wire will be generated by a combined source term which takes the values $-\mathbf{v}$ and $4\pi\mathbf{j}_{ant}$ in the respective domains. Since the Faraday law is valid in any case, we can write system (7) in the form

$$\nabla \times \mathbf{E} = -\frac{\partial \mathbf{B}}{\partial t}, \tag{8}$$
$$\nabla \times \mathbf{B} = -\mathbf{v}+4\pi\mathbf{j}_{ant},$$
$$\frac{\partial \mathbf{v}}{\partial t} + (\mathbf{v}\cdot\nabla)\,\mathbf{v} = -\mathbf{E} - \mathbf{v}\times\mathbf{B}-\nu\mathbf{v},$$

where $\mathbf{j}_{ant} = \lambda_e\mathbf{J}_{ant}/(B_* c)$ is the dimensionless current and $\mathbf{J}_{ant}$ is the dimensional current.

3.1 Decomposition of the fields

In order to avoid singularity in solution it is convenient to decompose the electric and magnetic field into components, which depend purely on the antenna input and computable additions. The former components can be precomputed or found at any given time without solving the whole system.

$$\mathbf{E} = \mathbf{E}_{ant} + \mathbf{E}', \quad \mathbf{B} = \mathbf{B}_0+\mathbf{B}_{ant} + \mathbf{B}', \quad \nabla\times\mathbf{B}_0 = \mathbf{0}, \quad \frac{\partial \mathbf{B}_0}{\partial t} = \mathbf{0}, \tag{9}$$

where we also included in decomposition a stationary irrotational background field $\mathbf{B}_0$ which has no singularity. Such decompositions can be selected more or less arbitrarily with the only requirement that $\mathbf{E}_{ant}$ and $\mathbf{B}_{ant}$ have the same singularity at the antenna location as the total fields. For example, one can use electric and magnetic fields in vacuum

$$\nabla\times\mathbf{B}_{ant} = 4\pi\mathbf{j}_{ant}, \quad \nabla\times\mathbf{E}_{ant} = -\frac{\partial \mathbf{B}_{ant}}{\partial t}. \tag{10}$$

The problem with such decomposition is that such fields decay relatively slowly (as solutions of the Laplace equation (not localized)), while the fields in plasma decay fast (as solutions of the screened potential equation (localized)). Hence, in this case as $\mathbf{E}$ and $\mathbf{B}$ should be localized in the region occupied by the waves, additions $\mathbf{E}'$ and $\mathbf{B}'$ should be not localized. Moreover, these additions should decay as solutions of the Laplace equation to compensate non-local behavior of $\mathbf{E}_{ant}$ and $\mathbf{B}_{ant}$. To avoid this problem we can introduce $\mathbf{E}_{ant}$ and $\mathbf{B}_{ant}$ as solutions of the screened potential equation, which has the same singularity.

The screened vector potential of antenna, $\mathbf{A}_{ant}$, from which $\mathbf{B}_{ant}$ and $\mathbf{E}_{ant}$ can be determined satisfies equation

$$\nabla \times \nabla \times \mathbf{A}_{ant} + \mathbf{A}_{ant} = 4\pi \mathbf{j}_{ant}, \quad \mathbf{B}_{ant} = \nabla \times \mathbf{A}_{ant}, \quad \mathbf{E}_{ant} = -\frac{\partial \mathbf{A}_{ant}}{\partial t}. \tag{11}$$

Substitution of Eqs (9) and (11) into Eq. (8) results in the system

$$\begin{aligned} \nabla \times \mathbf{E}' &= -\frac{\partial \mathbf{B}'}{\partial t}, \\ \nabla \times \mathbf{B}' &= -\mathbf{v} + \mathbf{A}_{ant}, \\ \frac{\partial \mathbf{v}}{\partial t} + (\mathbf{v} \cdot \nabla)\, \mathbf{v} &= -\mathbf{E}' - \mathbf{E}_{ant} - \mathbf{v} \times (\mathbf{B}_0 + \mathbf{B}_{ant} + \mathbf{B}') - \nu \mathbf{v}. \end{aligned} \tag{12}$$

3.2 Vector potential for loop antennas

Assume that the antenna consists of one or several closed loops. Since the latter case can be easily treated by superposition of the antenna vector potentials, it is sufficient to consider just a single loop C. In this case solution of Eq. (11) for current $I_{ant}(t)$ can be written in the integral form

$$\mathbf{A}_{ant}(\mathbf{r},t) = -4\pi I_{ant}(t) \int_C G(\mathbf{r}, \mathbf{r}')\, d\mathbf{l}(\mathbf{r}'), \tag{13}$$

where $\mathbf{l}(\mathbf{r}')$ is the vector element along contour C, and G is Green's function for the scalar equation

$$\begin{aligned} \nabla^2_{\mathbf{r}} G(\mathbf{r}, \mathbf{r}') - G(\mathbf{r}, \mathbf{r}') &= -\delta(\mathbf{r} - \mathbf{r}'), \\ G(\mathbf{r}, \mathbf{r}') &= \frac{e^{-r''}}{4\pi r''}, \quad \mathbf{r}'' = \mathbf{r} - \mathbf{r}'. \end{aligned} \tag{14}$$

In most cases the contour integral should be found numerically and stored (the same relates to the curl of this integral). After that $\mathbf{B}_{ant}$ and $\mathbf{E}_{ant}$ can be found from Eq. (11) simply by multiplication by respective factor $\sim I_{ant}(t)$ and $\sim \dot{I}_{ant}(t)$ as the time dependence of the antenna current is specified.

Note that when using spectral methods the potential $\mathbf{A}_{ant}(\mathbf{r},t)$ can be computed in the Fourier, or k-, space, which can simplify the computation or even provide an analytical expression

$$\mathbf{A}^*_{ant}(\mathbf{k},t) = \int_{\mathbb{R}^3} \mathbf{A}_{ant}(\mathbf{r},t)\, e^{-i\mathbf{k}\cdot\mathbf{r}} d\mathbf{r} = -\frac{4\pi}{k^2+1} I_{ant}(t) \int_C \mathbf{l}(\mathbf{r}')\, e^{-i\mathbf{k}\cdot\mathbf{r}'} dl(\mathbf{r}'), \tag{15}$$

which can be obtained from Eqs (13) and (14) since in the k-space

$$G^*(\mathbf{k}, \mathbf{r}') = \frac{e^{-i\mathbf{k}\cdot\mathbf{r}'}}{k^2+1}, \quad k = |\mathbf{k}|, \tag{16}$$

In Appendix A we provide analytical expression of this integral for a circular loop antenna.

4 Pseudospectral method

4.1 Computational form of basic equations

Convenient computational form of Eqs (7), which reduces the system to two elliptic and one evolutionary equation was obtained in [6]. A similar transform can be applied to Eq. (12). Indeed, taking into account

Eq. (11) we obtain from the first two equations (12)

$$\frac{\partial \mathbf{v}}{\partial t} = \nabla \times \nabla \times \mathbf{E}' - \mathbf{E}_{ant}. \tag{17}$$

Substituting this into the third equation (12) we have

$$\nabla \times \nabla \times \mathbf{E}' + \mathbf{E}' = -\left(\mathbf{v} \cdot \nabla\right) \mathbf{v} - \mathbf{v} \times \left(\mathbf{B}_0 + \mathbf{B}_{ant} + \mathbf{B}'\right) - \nu \mathbf{v}. \tag{18}$$

In principle, a pseudospectral method can be applied immediately to solve these equations, plus the second equation (12) as it is done in [6]. However, if explicit time integration occurs in the real space and $\nabla \times \nabla \times \mathbf{E}'$ should be computed using spectral solver for Eq. (18) with the right hand side known from the previous time step, it is not difficult to count that evaluation of $\nabla \times \nabla \times \mathbf{E}'$ requires 21 FFTs (including forward and inverse transforms) (indeed tensor $\nabla \mathbf{v}$ has 9 components). This can be reduced to 18 FFTs if time integration will be performed in the k-space. In fact, this can be reduced only to 9 FFTs using the following transform.

Due to $\nabla \cdot \mathbf{v} = 0$ the convective term can be written as

$$\left(\mathbf{v} \cdot \nabla\right) \mathbf{v} = \nabla \frac{v^2}{2} - \mathbf{v} \times \left(\nabla \times \mathbf{v}\right), \quad v^2 = \mathbf{v} \cdot \mathbf{v}. \tag{19}$$

Hence, using the second equation (12) and the second equation (11), we obtain the following form of equation (18):

$$\nabla \times \nabla \times \mathbf{E}'' + \mathbf{E}'' = -\mathbf{h} - \nu \mathbf{v}, \quad \left(\nabla^2 - 1\right) \nabla \times \nabla \times \mathbf{E}'' = \nabla \times \nabla \times \mathbf{h} - \nu \nabla^2 \mathbf{v}, \tag{20}$$

$$\mathbf{E}' = \mathbf{E}'' - \nabla \frac{v^2}{2}, \quad \nabla \times \nabla \times \mathbf{E}' = \nabla \times \nabla \times \mathbf{E}'',$$

where

$$\mathbf{h} = \mathbf{v} \times \left(\mathbf{B}_0 + \mathbf{b}\right), \quad \mathbf{b} = \mathbf{B}' - \nabla^2 \mathbf{B}'. \tag{21}$$

Note that the second equation (12) yields

$$\nabla \times \mathbf{b} = \left(\nabla^2 - 1\right) \mathbf{v} - \left(\nabla^2 - 1\right) \mathbf{A}_{ant}. \tag{22}$$

This shows that if time integration occurs in the k-space only 9 FFTs are needed to convolve the nonlinear term in the real space (6 inverse FFTs for components of vectors $\mathbf{b}$ and $\mathbf{v}$ and 3 forward FFTs for components of vector $\mathbf{h}$). Indeed, full system in the k-space ($\nabla \to i\mathbf{k}$) can be written as

$$\begin{aligned} \frac{\partial \mathbf{v}^*}{\partial t} &= \frac{1}{1+k^2} \mathbf{k} \times \mathbf{k} \times \mathbf{h}^* - \frac{\nu k^2}{1+k^2} \mathbf{v}^* - \mathbf{E}^*_{ant}, \\ \mathbf{b}^* &= \frac{1+k^2}{k^2} \left(-i\mathbf{k} \times \mathbf{v}^* + \mathbf{B}^*_{ant}\right), \\ \mathbf{h}^* &= \left[\mathbf{v} \times \left(\mathbf{B}_0 + \mathbf{b}\right)\right]^*. \end{aligned} \tag{23}$$

4.2 Advancing in time

4.2.1 Explicit schemes

In the k-space evolutionary equation (23) can be treated as a large system of ODEs which can be solved using any stable and accurate method. Due to the nonlinearity the use of fully implicit schemes is computationally inefficient and standard high order explicit integrators, such as Adams-Bashforth (AB) or Adams-Bashforth-Moulton (ABM) predictor-corrector schemes can be used (see e.g. [11]). For appropriate time steps these methods are absolutely stable, while A-unstable [11], which manifests itself only at sufficiently large times.

In [7] the leap-frog predictor and trapezoidal corrector was used and in [6] a predictor-corrector-corrector scheme of better stability properties, which requires 3 evaluations of the right hand side per time step, was proposed. The latter scheme is a modified Runge-Kutta 3rd order integrator, where coefficients are selected

to damp term $O\left(h^4\right)$, which reduces the accuracy to the second order, since it is impossible in this case to damp the term $O\left(h^3\right)$ (while the asymptotic coefficient for this term, 1/24, is small enough). Similar order of accuracy for the wave amplitude can be achieved using the AB 4th order (AB4) and ABM 4th order schemes (ABM4), which require 1 and 2 right hand side evaluations. In contrast to the scheme [6] they provide the same order of accuracy for the amplitude and phase of the wave. Higher order schemes, such as AB6 and ABM6 have the same computational cost (with some increase in memory) as AB4 and ABM4, while provide more accurate computations.

We have implemented all these schemes and found them satisfactory, while the most accurate computations were performed using additional iteration of the nonlinear term each time step. For such a scheme AB6 was used as a predictor, and then the Moulton correction (ABM6) was applied several times until the iteration error reaches some prescribed value. The number of such iterations is usually small (in average we had not more than 3 iterations), while this allows to integrate with relatively large time step (several times larger than with AB4 for the same accuracy) and the scheme becomes much more stable. As a result overall saving in computation time was achieved for substantially nonlinear cases.

4.2.2 Analogy with the Navier-Stokes equations

We note that integration of fully nonlinear system is a complex task, which is not less than solution of the Navier-Stokes equations for incompressible liquid. It is not difficult to show (see transforms (17)-(22), also [12]) that the initial system (7) can be reformulated in terms of vorticity $\boldsymbol{\omega}$ as

$$\begin{gathered}\frac{\partial \boldsymbol{\omega}}{\partial t}+(\mathbf{v}\cdot\nabla)\,\boldsymbol{\omega}-(\boldsymbol{\omega}\cdot\nabla)\,\mathbf{v}=\nu\left(1-\nabla^2\right)^{-1}\nabla^2\boldsymbol{\omega}, \\ \nabla^2\boldsymbol{\omega}=\left(1-\nabla^2\right)\nabla\times\mathbf{v},\quad \nabla\cdot\boldsymbol{\omega}=\nabla\cdot\mathbf{v}=0, \\ \left(\boldsymbol{\omega}=\mathbf{B}-\nabla^2\mathbf{B},\quad \nabla^2\mathbf{B}_0=\mathbf{0}\right).\end{gathered} \tag{24}$$

Indeed, since dissipation ν is usually very small (high Reynolds numbers) and the diffusion of the vorticity $\boldsymbol{\omega}$ is small, the vorticity propagates similarly to that in the inviscid vortical flow. The difference comes in the relation between $\boldsymbol{\omega}$ and $\mathbf{v}$, which anyway has an elliptic nature, as in fluid motion. This relation shows that for small scales $\left(k^2\gg 1,\quad \nabla^2\gg 1\right)$ we have $\boldsymbol{\omega}=-\nabla\times\mathbf{v}$, which results in a complete analogy with the incompressible liquid motion (except of the dissipation term, which will be $-\nu\boldsymbol{\omega}$ instead of $\nu\nabla^2\boldsymbol{\omega}$). For large scales $\left(k^2\ll 1,\quad \nabla^2\ll 1\right)$ the dissipative term will be the same as for liquid, while $\nabla\times\mathbf{v}=\nabla^2\boldsymbol{\omega}\ll\boldsymbol{\omega}$, which shows that the velocity field in our case will be different from that in the case of fluid. In any case the above system shows that numerical methods used for integration of vortical flows can be directly applied to the solution of the present problem as the major difference come only in the elliptic relation between the velocity and vorticity. Particularly, this is important for large amplitude perturbations , where one can expect highly developed turbulent flows at small scales (e.g. Lagrangian and particle methods can be employed [13] instead of pseudospectral techniques [11]). For small amplitude perturbations the major contribution to $\boldsymbol{\omega}$ will be due to the background field $\mathbf{B}_0$, which, therefore causes vortical motion even for zero dissipation and small amplitudes (similarly to free vortices in an inviscid fluid).

4.2.3 Linearly stable scheme

For the problem considered, the integrator can be made stable for the linear problem, moreover for a special, but practically important case solution can be obtained analytically. Also the system can be transformed to a form, which is more compact in memory, which allows one to compute and store only two scalar variables per time step, as all components of vectors can be derived from this.

Indeed, the background magnetic field can be decomposed as

$$\mathbf{B}_0=\mathbf{B}_{00}+\mathbf{B}_0',\quad \mathbf{B}_{00}=\mathbf{i}_z,\quad \left(\mathbf{B}_0'\right)^*\big|_{k=0}=0, \tag{25}$$

where $\mathbf{B}_{00}$ is a constant component, which without loss of generality can be assumed oriented along the z-axis and its amplitude can be set to 1 in the dimensionless form, and $\mathbf{B}_0'$ is the component with zero spatial mean value (its Fourier component at $\mathbf{k}=\mathbf{0}$ is zero). We also note that mean values of vectors $\mathbf{b}$

and $\mathbf{v}$ are zeros, so vector $\mathbf{h}$ in Eq. (21) can be represented as

$$\mathbf{h} = \mathbf{g} + \mathbf{v} \times \mathbf{i}_z, \quad \mathbf{g} = \mathbf{v} \times \left(\mathbf{b} + \mathbf{B}_0'\right). \tag{26}$$

The first equation (23) now can be written as

$$\frac{\partial \mathbf{v}^*}{\partial t} = \frac{1}{1+k^2}\mathbf{k} \times \mathbf{k} \times (\mathbf{v}^* \times \mathbf{i}_z) - \frac{\nu k^2}{1+k^2}\mathbf{v}^* - \mathbf{E}_{ant}^* + \frac{1}{1+k^2}\mathbf{k} \times \mathbf{k} \times \mathbf{g}^*, \tag{27}$$

where two first terms in the right hand side form a linear part of the system as mode $\mathbf{k}$ determines evolution of the same mode, $-\mathbf{E}_{ant}^*$ is the external driving term, while the last term is completely due to non-uniformity of the background magnetic field and nonlinearity. If $\mathbf{B}_0' = \mathbf{0}$ and amplitude of disturbances is small, this term is small, and the system is close to a linear system. Otherwise, we note that for a given timestep linearization of this term results in a system matrix with all mode interaction, but there is no immediate self-action of mode $\mathbf{k}$ (by construction of $\mathbf{g}$). This means that, even in a general case, the system matrix based on the Jacobian has diagonal elements determined only by the linear term, while interaction between the modes comes via the off-diagonal elements.

Furthermore, due to zero divergence of $\mathbf{v}$, which means $\mathbf{k} \cdot \mathbf{v}^* = \mathbf{0}$ the three components of $\mathbf{v}^*$ are linearly dependent, and complete information on $\mathbf{v}^*$ can be obtained via only two scalar variables. Such variables come naturally if we introduce spherical coordinates in the k-space

$$\mathbf{k} = (k_x, k_y, k_z) = k\left(\sin\theta_k \cos\varphi_k, \sin\theta_k \sin\varphi_k, \cos\theta_k\right). \tag{28}$$

Hence if an arbitrary vector $\mathbf{F}^*$ has coordinates $\left(F_k^*, F_{\theta_k}^*, F_{\varphi_k}^*\right)$, then a divergence free vector is $\mathbf{F}^* = \left(0, F_{\theta_k}^*, F_{\varphi_k}^*\right)$. In fact, the linear system can be completely diagonalized in a complex basis. Indeed, denoting

$$F_+^* = F_{\theta_k}^* + iF_{\varphi_k}^*, \quad F_-^* = F_{\theta_k}^* - iF_{\varphi_k}^*, \tag{29}$$

for an arbitrary vector, we obtain

$$\begin{aligned}
\frac{\partial v_+^*}{\partial t} &= -\frac{k}{1+k^2}\left(\nu k - ik_z\right)v_+^* - E_{ant,+}^* - \frac{k^2}{1+k^2}g_+^*, \\
\frac{\partial v_-^*}{\partial t} &= -\frac{k}{1+k^2}\left(\nu k + ik_z\right)v_-^* - E_{ant,-}^* - \frac{k^2}{1+k^2}g_-^*, \\
b_+^* &= \frac{1+k^2}{k}v_+^*, \quad b_-^* = -\frac{1+k^2}{k}v_-^*.
\end{aligned} \tag{30}$$

In the linear case this form provides easy analytical solution for a given wavevector $\mathbf{k}$

$$v_\pm^*(\mathbf{k}, t) = e^{\lambda_\pm t}\left[v_\pm^*(\mathbf{k}, 0) - \int_0^t e^{-\lambda_\pm t'} E_{ant,\pm}^*(\mathbf{k}, t')\, dt'\right], \tag{31}$$

where the eigenvalues are

$$\lambda_\pm(\mathbf{k}) = -\frac{\nu k^2}{1+k^2} \pm i\frac{kk_z}{1+k^2}, \tag{32}$$

which are consistent with that obtained in [9]. Such solution is especially efficient when the driving field can be factored. For example, for N_{ant} antennas we have

$$\mathbf{E}_{ant}^*(\mathbf{k}, t) = \sum_{n=1}^{N_{ant}} I^{(n)}(t)\widehat{\mathbf{E}}_{ant}^{(n)*}(\mathbf{k}), \tag{33}$$

and time integrals involve computation of prescribed functions $I^{(n)}(t)$, which can be done analytically or numerically for all modes at once. Obviously, the eigenvalues provide linear dispersion relationship for the whistler waves, which is consistent (at zero dissipation) discussed in [15], [6]:

$$\omega_\pm(\mathbf{k}) = -i\lambda_\pm(\mathbf{k}). \tag{34}$$

Equations (30) also suggest an efficient numerical scheme of solution using integrating factor technique (e.g. [11], [16]). In this case instead of state variables $v^*_\pm(\mathbf{k},t)$ we use variables $C^*_\pm(\mathbf{k},t) = e^{-\lambda_\pm t} v^*_\pm(\mathbf{k},t)$. Since these variables satisfy equations

$$\frac{\partial C^*_\pm}{\partial t} = -e^{-\lambda_\pm t}\left(E^*_{ant,\pm} + \frac{k^2}{1+k^2} g^*_\pm\right), \quad v^*_\pm(\mathbf{k},t) = e^{\lambda_\pm t} C^*_\pm(\mathbf{k},t), \tag{35}$$

the method is unconditionally stable for $g^*_\pm = 0$ and any instability can be related only to the nonlinearity and the non-uniformity of the background magnetic field. Equations (35) can be solved numerically by any of the explicit methods described above.

The unconditional stability for a nonlinear system can be expected only if the nonlinear term is small enough and the eigen values of the total system are close to the values on the main diagonal. For higher amplitudes explicit treatment of nonlinearity should result in instabilities, which in the present algorithm can only be treated by reduction of the time step. However the use of the integrating factor somehow "reduces the stiffness" of the system and stabilizes numerical solution for small and moderate amplitudes. Here we should also mention study [14] who proposed to separate the spectrum into three ranges and apply different time integration schemes for different parts of spectra when solving the Korteweg-de-Vries equation. This paper as well as a number of papers, also considers time-splitting methods, which work well for relatively simple nonlinear evolution equations, such as nonlinear Schroedinger and KdV, as the split system have analytical solutions in the real or Fourier space. The present system is as complex as, say, fully nonlinear 3D Navier-Stokes equations and implementation of accurate time-splitting schemes requires more research, while some ideas can be borrowed from already developed techniques [11], [16].

In the present algortihm we also used dealiasing based on the 2/3 rule (e.g. [11], [16]). Note here that dealiasing when time integration is performed in the Fourier space is benefitial in terms of memory and speed as it shrinks the size of state variables.

4.3 Implementation

The algorithm was implemented under MATLAB environment, which is efficient for the present problem as provides a good performance FFT library, while all operations in the algorithm can be vectorized. This environment also allows a user to easily map the algorithm on the graphic processors using AccelerEyes Jacket interface, which supports basic MATLAB operations and interfaces with the CUFFT library. In terms of the FFT we use half-size storage in the Fourier space (due to real symmetry) and modified the IFFT/FFT routines in a way that they automatically provide zero-padding or spectral truncations based on the 2/3 rule.

5 Numerical tests

Numerical tests were performed on a standard 3GHz PC with 8GB RAM and NVIDIA graphic card Tesla 1060 (4GB RAM) with varying grid size, input fields, antenna configurations, and time steps. Several integration schemes were tested and performance of the code was measured in terms of speed and memory.

5.1 Example computations

5.1.1 Linear waves induced by antennas

Several computations were performed using a linear code, which also was compared with the analytical solution for inputs from one or two loop antennas (see Eq. (33)). Fig. 1 illustrates distribution of the y-component of the magnetic field for one loop antenna in the center plane ($y = 0$) at $t = 375$ as a function of x and z. The radiating antenna of radius $a = 2.65$ was placed in the xz-plane and co-centered with the origin of the reference frame. The excitation started at $t = 0$ and the driving antenna at $t > 0$ current was $I(t) = I_0 \cos\omega_{ext} t$, with $I_0 = 0.001$ and $\omega_{ext} = 0.04$. Computational domain of size $125 \times 125 \times 500$ was discretized by $256 \times 256 \times 512$ grid. Fig. 1 shows that the linear analytical solution obtained from (31) is close to the numerical solution of the full nonlinear system obtained using integration with time step $h = 1/4$ and the relative magnitude of the nonlinear effects in this case can be estimated as $\sim 10^{-2}$ (in the L_2-norm

the difference between the linear and nonlinear solutions is about $4 \cdot 10^{-3}$ which is consistent with the order of the perturbation magnitude).

More validation tests were performed for the same domain size by changing the grid sizes and convergence was observed for increasing number of grid points (e.g., computations on the grid $128 \times 128 \times 256$ for the case illustrated in Fig. 1 had 10% of relative error with respect to the reference solution on $256 \times 256 \times 512$ grid, while computations on $256 \times 256 \times 256$ grid had 1% of the relative error with respect to the reference solution). The tests also were performed for different time steps on the same grid. In this case a solution obtained on a CPU with double precision and $h = 1/32$ served as a reference. A decrease of the time step from $h = 1/2$ to $h = 1/8$ both for the CPU and GPU (single precision) computations showed that the relative error reduces 16 times as h is halved, which is consistent with the accuracy of the AB4 scheme used. This trend continues for $h = 1/16$ for CPU computations, but stops at this value for the GPU as the single precision limit is reached. So a reduction of the time step for the GPU below $h = 1/16$ had almost no effect on the relative error, which stabilized around 10^{-6}.

Figure 2 shows a comparison between the computed and experimentally measured rotating magnetic fields [4], [5] generated by a two loop antenna, where the experiments were conducted in the conditions for which linear approximation should be acceptable. Here the imaging plane is taken to be a z-slice (xy-plane at some z). It is seen that computations reproduce features of the field observed in the experiment and provide a correct magnitude of the field. Some differences are also observed, which are due to different geometry of the experimental and computational domains (in the experiments it was a tube), plus in the experiments the plasma density was weakly inhomogeneous, while in the computations this effect was neglected.

5.1.2 Nonlinear waves induced by antennas

To study the effects of nonlinearity we performed several test runs for two-loop antennas with the parameters close to the experiments, but with different magnitudes of the input currents. In these computations, the domain had sizes $67.6 \times 67.6 \times 270.3$, which was discretized by $150 \times 150 \times 600$ grid. The driving frequency was $\omega_{drive} = 0.1$ and the currents in the loops had the same magnitude I_0 and were oscillating with $\pi/2$ phase shift as in the case described above (the diameter of the loops also was the same, $a = 2.65$).

Figure 3 illustrates the results for the magnetic field, $\mathbf{B}'$. The panels in the left column show that at low input current magnitudes, the whistler waves have a regular structure (see also Fig. 1). The increase of the amplitude leads to distortion of this structure, which at larger amplitudes looses its regularity and forms turbulent structures propagating from the source in the $\pm z$ directions. The panels in the right column show the z-slices of the magnetic field. The rotating structure of the field is clearly seen. It is also seen that large amplitude of the nonlinearity leads to a more complex structure.

We note that in all computations we varied the time step for integration to achieve stable reproducible results. While for the linear case the time integration step could be as large as $h = 1/4$ (or even larger), substantial reduction of the time step were needed to achieve stable computations for substantially nonlinear cases. The fact that the time step should be reduced at increasing non-linearity has an easy explanation. Indeed, the electron cyclotron frequency Ω_e increases proportionally to the scale B_*. If this scale is taken to be B_0 (background), this is the true scale only for low amplitude perturbations. As the amplitude of the field increases, the effective cyclotron frequency increases as well. Since in our scaling we fixed Ω_e to be determined by the background amplitude, we at least should decrease the time step inversely linearly with the amplitude of the field to provide the same stability conditions for larger amplitude perturbations as for the case of small amplitudes. For example, we found that computations for amplitude $I_0 = 5$ required integration time step $h = 1/32$ for stable computations for a given time interval ($0 < t < 500$).

5.1.3 Spheromak-like structures

It was found experimentally (e.g. [17]) and confirmed numerically [8] that there exist localized whistler-mode wave packets where the amplitudes of the fields exceed the ambient magnetic field. In [8] modeling was performed using basic equations (1), which were reduced to a single nonlinear evolution equation for magnetic field using transforms (17)-(22). This equation was solved using a pseudospectral method with Runge-Kutta time marching in real space. For a test we used the same initial conditions as provided in [8] and compared results with [8], which showed consistency and a good agreement with experiment.

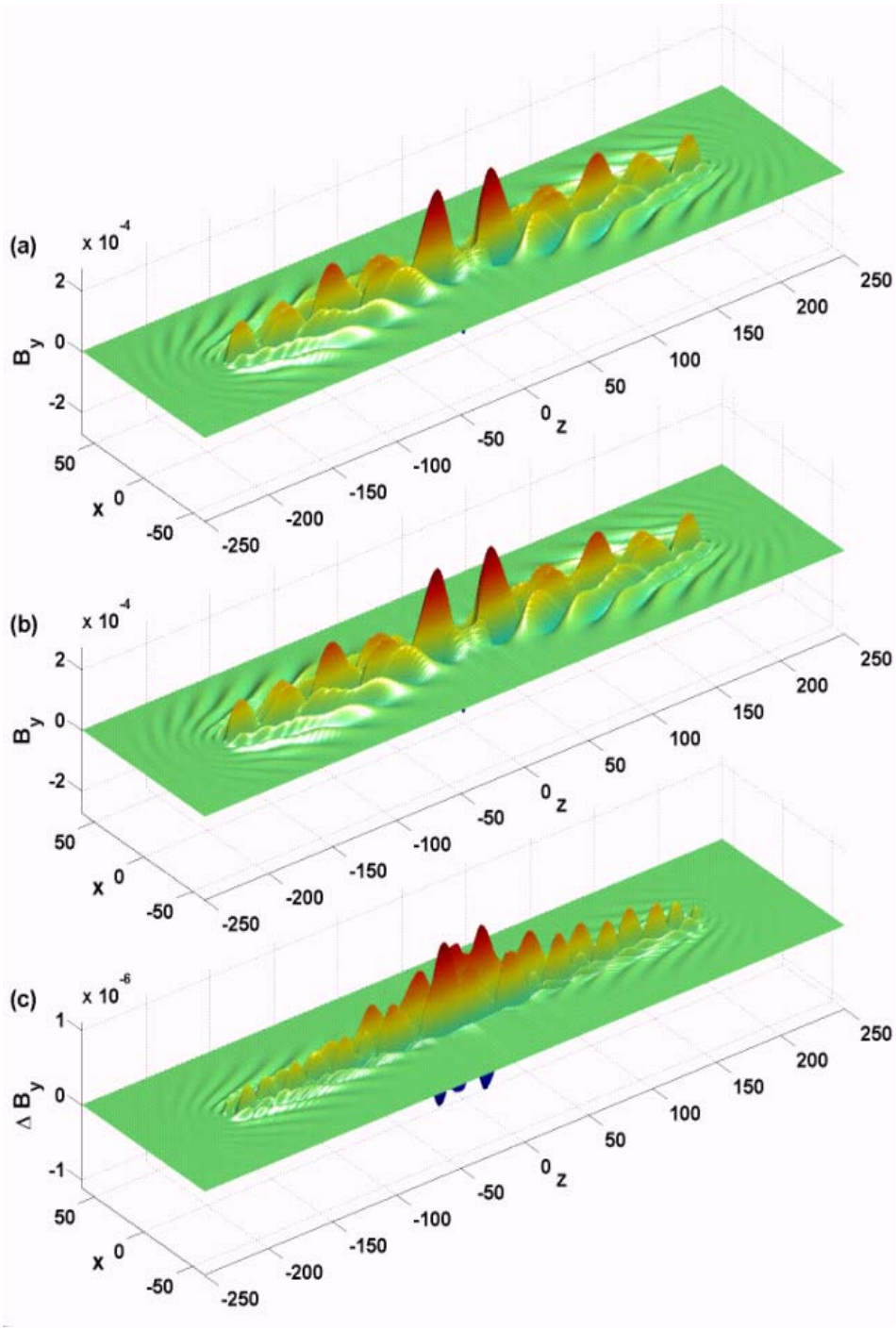

Figure 1: Comparison of the analytical solution of the linear problem with the numerical solution of fully nonlinear problem for waves introduced by a one loop antenna driven by a small amplitude current $I_0 = 0.001$ ($B_y(x, y, z, t)$, $y = 0$, $t = 375$) driven at frequency $\omega_{ext} = 0.04$. Plot (c) shows the absolute difference between the analytical (a) and the numerical (b) solutions.

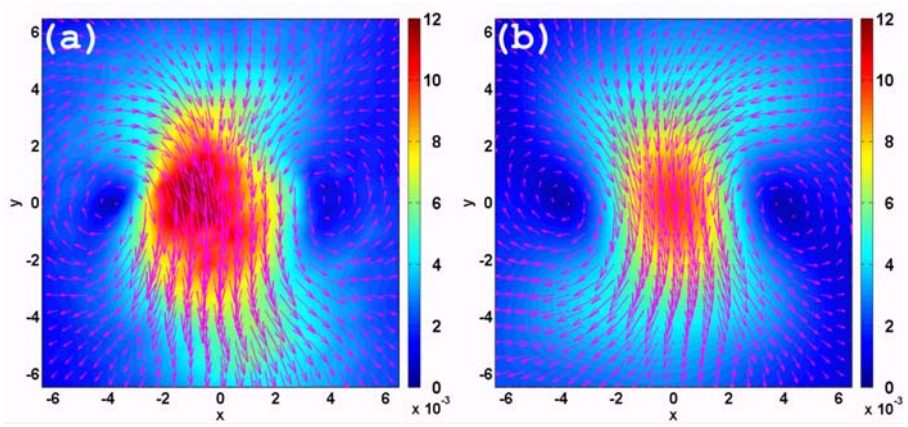

Figure 2: Comparison of the computated (b) and measured in experiments (a) magnetic fields at section $z = 46.5$. The wave was generated by a two-loop antenna ($a = 2.45$) by current $I_1 = I_2 = 0.141$ of frequency ω_{drive}=0.002 with $\pi/2$ phase difference between loops 1 and 2. Collision frequency $\nu = 0.007$. Computational domain 324×324×1276 was discretized by grid $324 \times 324 \times 638$. The arrows show $\left(B'_x, B'_y\right)$ vector field and the color shows the amplitude of the normal component of the magnetic field.

The works cited above are related to structures called spheromaks, which are toroidal magnetic vortices oriented in the way that the torus axis is directed along (or opposite) to the constant background magnetic field $\mathbf{B}_0 = \mathbf{i}_z$. In this case the 3D fields depend only on 2 spatial coordinates (z, and $\rho = \left(x^2 + y^2\right)^{1/2}$), which can be used to simplify computations. Below we present an analytical solution of fully nonlinear equations in more general settings, which show that similar structures can be designed in a very broad range for arbitrary amplitudes of perturbations.

Analytical solution In fact, the analytical solution for this case is such that solution of the linear system coincides with the solution of the nonlinear system. This is possible if

$$\mathbf{v} \times \mathbf{b} = \mathbf{0}, \tag{36}$$

and nonlinearity in (21) disappears. This corresponds to the force-free configurations [18], [19]. In this case for constant background magnetic field $\mathbf{B}_0 = \mathbf{i}_z$ solution is described by Eqs (30)-(31), where one should set $E^*_{ant,\pm} = g^*_{\pm} = 0$. It is not difficult to find then that there exist a stationary solution traveling with a constant speed, $\mathbf{v}\,(x, y, z, t) = \mathbf{V}(x, y, z - ct)$, which should satisfy equation

$$c\mathbf{b} = -\mathbf{v}, \tag{37}$$

or, as follows from Eq. (22)

$$c\left(\nabla^2 - 1\right)\mathbf{v} + \nabla \times \mathbf{v} = \mathbf{0}. \tag{38}$$

Obviously, if (37) holds then (36) holds as well. This equation can be diagonalized if we take the curl of this equation, take into account that $\nabla \cdot \mathbf{v} = 0$, and use Eq. (38) to get rid of the $\nabla\times$ operator:

$$\left[c^2\left(\nabla^2 - 1\right)^2 + \nabla^2\right]\mathbf{v} = \mathbf{0}. \tag{39}$$

Note that in this case we introduce an additional solution for $-c$, which corresponds to the wave propagating in the opposite direction. So care should be taken to separate the two ($\pm$) solution to have a single wave.

Eq. (39) is a linear elliptic equation, which can be solved using standard methods as soon as some boundary conditions are provided. To generate non-trivial solutions decaying at infinity, we can replace the

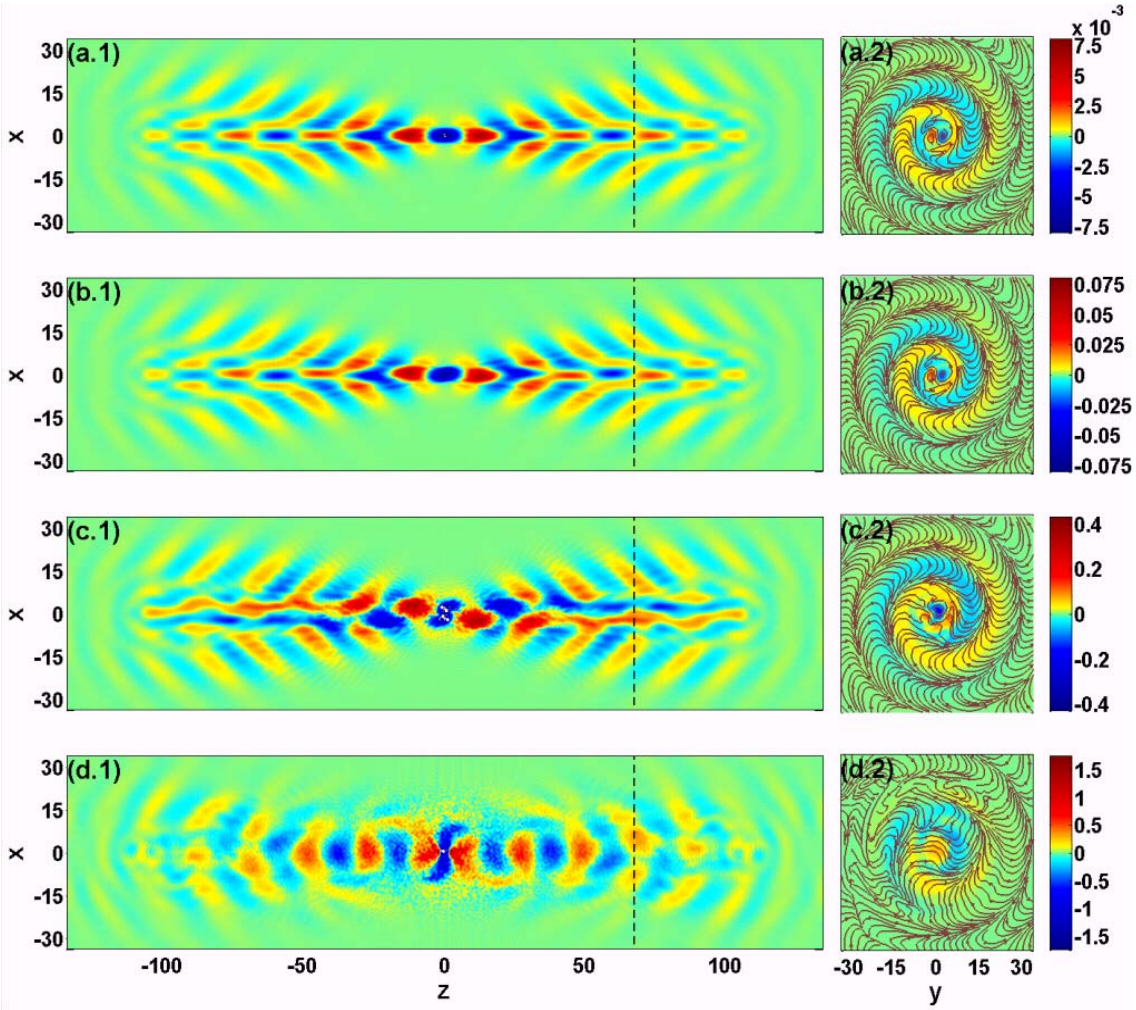

Figure 3: Computations of waves of different degree of the nonlinearity generated by a two loop antenna (right handed polarization) driven with currents oscillating with frequency $\omega_{drive} = 0.1$ and having magnitudes $I_0 = 0.005, 0.05, 0.5$, and 5 (cases a, b, c, and d, respectively). The charts $(a.1)$-$(d.1)$ show B'_y at $t = 220$. The streamlines on charts $(a.2)$-$(d.2)$ show projection of the magnetic field perturbation $\left(B'_x, B'_y\right)$ on the imaging plane at constant z, which location is shown by the dashed lines on charts $(a.1)$-$(d.1)$. The color on charts $(a.2)$-$(d.2)$ shows B'_z component.

right hand side with some singularity. Particularly, we can construct a scalar Green's function as a solution of equation

$$\left[c^2\left(1-\nabla_{\mathbf{r}}^2\right)^2+\nabla_{\mathbf{r}}^2\right]G\left(\mathbf{r},\mathbf{r}'\right)=-\delta\left(\mathbf{r},\mathbf{r}'\right). \tag{40}$$

Consider now a closed loop C (vortex core) with a vector element $\mathbf{l}\left(\mathbf{r}'\right)$ at a given point $\mathbf{r}'$. In this case divergence free vector field $\mathbf{v}$ satisfying Eq. (39) everywhere (except of the singularity at C) generated by a current of intensity I can be found from

$$\mathbf{v}\left(\mathbf{r}\right)=-4\pi I\int_C\mathbf{l}\left(\mathbf{r}'\right)G\left(\mathbf{r},\mathbf{r}'\right)dl\left(\mathbf{r}'\right). \tag{41}$$

In the Fourier space this turns into

$$\mathbf{v}^*\left(\mathbf{k}\right)=\frac{4\pi I}{c^2\left(k^2+1\right)^2-k^2}\int_C\mathbf{l}\left(\mathbf{r}'\right)e^{-i\mathbf{k}\cdot\mathbf{r}'}dl\left(\mathbf{r}'\right), \tag{42}$$

and computation of the integral and construction of the solution is similar to the construction of the vector potential for loop antennas (e.g. see Appendix A).

As we mentioned above only a single wave should be extracted from this solution. In fact, we can turn attention to variables $\nu_{\pm}^*$ which for stationary waves should satisfy equations

$$\left[c\left(1+k^2\right)+k\right]v_+^*=0,\quad \left[c\left(1+k^2\right)-k\right]v_-^*=0, \tag{43}$$

to find that for the wave propagating to the right ($c>0$) we should have to set $v_+^*=0$. Numerically, extraction of appropriate solution can be done as follows. First, compute $\mathbf{v}^*\left(\mathbf{k}\right)$ according to (42). Second, find v_+^* and v_-^* (see 29). Third, set $v_+^*=0$. Fourth, find $\mathbf{v}\left(\mathbf{r}\right)$ from components $v_{\pm}^*$.

Numerical solution We note that due to the presence of the source and finite set of discrete wavenumbers the right hand side of equation (43) is not zero. Due to this, time evolution of the spectrum does not correspond exactly to the translation. So we used a "cleaning" procedure for initial conditions, which is an iterative process aimed to enforce this equation for a finite spectrum:

$$v_{\pm}^{*(n+1)}\left(\mathbf{k},0\right)=\mp\frac{k}{c\left(1+k^2\right)}v_{\pm}^{*(n)}\left(\mathbf{k},0\right),\quad n=0,...,N, \tag{44}$$

where n is the iteration step and the process starts with the analytical solution (for infinite domain). Since this is a linear process it should necessarily end with zero or infinity, depending on the norm of operator $k/\left[c\left(1+k^2\right)\right]$. So, we applied renormalization in the L_∞ norm after each iteration to preserve the norm of the solution. Usually we performed 30-100 iterations. Note that this process is aimed only at creating a proper initial distribution $v_-^*\left(\mathbf{k},0\right)$, and after such a distribution was generated the code was executed without any modifications.

Figure 4 shows propagation of a structure whose initial state was generated by the procedure described above at $c=0.51$. While the amplitude of the field is large enough the structure showed stability at long times (thousands of integration time steps), after which it was destabilized (due to accumulation of long term nonlinear instability). The linear solution coincided with the non-linear solution for a long time, and was never destabilized. The test clearly confirmed existence of the stationary solution during the physically reasonable times. Figure 5 shows the 3D structure of magnetic field for a spheromak-type solution as in Fig. 4, but for a vortex core of radius $a=2\pi$.

Note that we computed more cases of stationary waves with different vortex core orientations, packets of such waves, etc. In all cases the present code when being set properly showed good stability and performance, which yielded physically explainable results. We also note that in all substantially nonlinear cases we observed destabilization of the stationary structures at large enough times (normally thousands of time steps), which is an indication of a long term instability of the present method. It is interesting that despite trying different values of parameter $c>0.5$, which is the velocity of the structure, this only changed the distributions, but

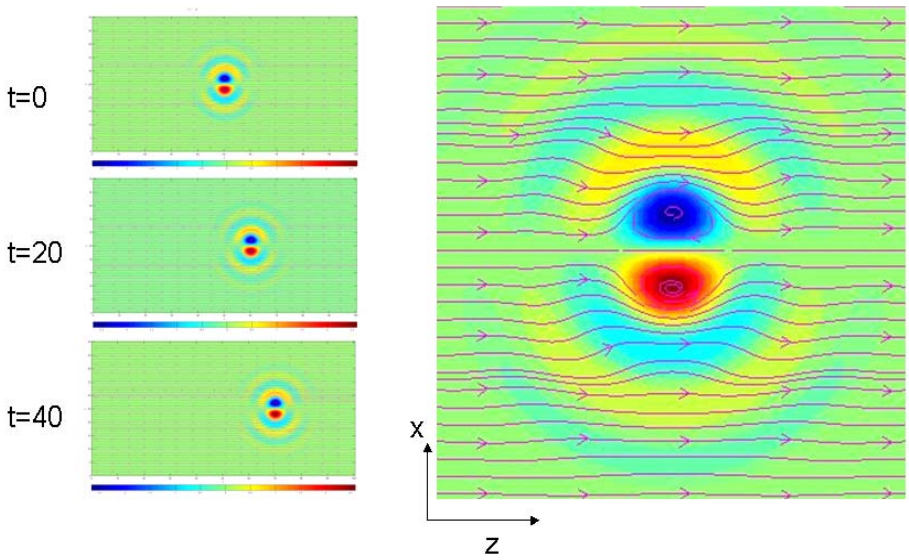

Figure 4: A stationary traveling solution for a whistler wave of max amplitude ˜4, generated by a ring with the moment along the z-axis (toroidal vortex). Radius of the loop is $a = \pi/2$. Colors show the y-component of the total magnetic field (B_y) in the center plane. The streamlines show (B_x, B_z) vector field in this plane.

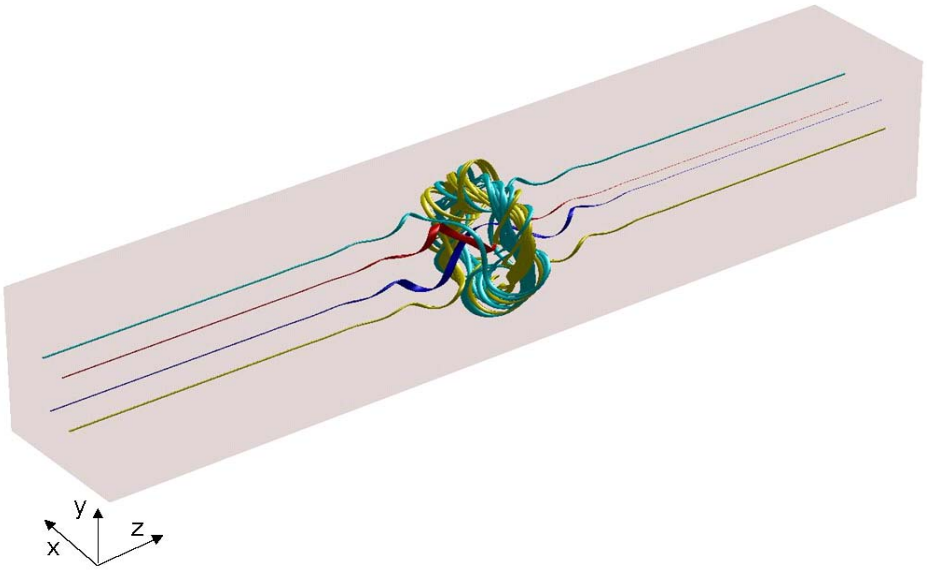

Figure 5: A stationary traveling solution for a whistler wave, generated by a ring with the moment along the z-axis. Radius of the loop is $a = 2\pi$. Stream tubes visualize total magnetic field $\mathbf{B}$.

all structures travelled with $c = 0.5$. There is an explanation for this fact. First, the second equation (43) has non-trivial solutions (k is real and non-negative) only at $c \leqslant 0.5$. Second, it can be shown that the phase and group velocities of the waves coincide only at $k = 1$, and $c = 0.5$. In the dispersive system these two velocities should coincide to provide a stationary wave structure for wave packets. Note that in the 3D case condition $k = 1$ is not very restrictive and provides enough room to construct a class of non-trivial solutions $v_-^*(k_x, k_y, k_z)$, for which $k_x^2 + k_y^2 + k_z^2 = 1$ (solutions of the Helmholtz equation).

5.1.4 Error tests

To check the accuracy of the simulations with the present algorithm on the CPU (double precision) and GPU (single precision) we performed error tests. In these tests we compared numerical and analytical (exact) solutions. To generate an exact solution of the nonlinear equations we used the following method, assuming that a solution of linear equations is known (e.g., it is given by Eq. (31)).

Indeed, Eq. (27) shows that the system can be written in the form

$$\frac{\partial \mathbf{v}^*}{\partial t} = \mathbf{L}(\mathbf{v}^*) + \mathbf{N}(\mathbf{v}^*) - \mathbf{E}_{ant}^*(t), \tag{45}$$

where $\mathbf{L}$ and $\mathbf{N}$ are linear and nonlinear operators acting on the solution and the forcing term $\mathbf{E}_{ant}^*$ is known at any moment of time. Assume now that a solution of the linear system, $\mathbf{v}_{lin}^*(t)$, driven by $\mathbf{E}_{ant}^*(t)$ is the solution of the nonlinear system, driven by an effective field $\mathbf{E}_{ant}^{(eff)*}(t)$. In this case we have

$$\frac{\partial \mathbf{v}^*}{\partial t} = \mathbf{L}(\mathbf{v}^*) + \mathbf{N}(\mathbf{v}^*) - \mathbf{E}_{ant}^{(eff)*}(t), \quad \frac{\partial \mathbf{v}_{lin}^*}{\partial t} = \mathbf{L}(\mathbf{v}_{lin}^*) - \mathbf{E}_{ant}^*(t), \quad \mathbf{v}^* = \mathbf{v}_{lin}^*. \tag{46}$$

Subtracting one equation from the other and taking into account $\mathbf{v}^* = \mathbf{v}_{lin}^*$, we can find that the effective field is

$$\mathbf{E}_{ant}^{(eff)*}(t) = \mathbf{E}_{ant}^*(t) + \mathbf{N}(\mathbf{v}_{lin}^*(t)). \tag{47}$$

Hence, if we solve numerically the first equation (46) with the same initial conditions as for the linear case and the driving field provided by Eq. (47) ideally we should reproduce the linear solution. Numerical error in the real space then can be computed as

$$\epsilon = \frac{\|\mathbf{v} - \mathbf{v}_{lin}\|}{\|\mathbf{v}_{lin}\|}. \tag{48}$$

In our tests we took the norm in L^∞ (relative maximum absolute error).

Figure 6 shows evolution of the errors for the test problem for GPU and CPU computations. In all cases the reference solution was computed on CPU with double precision. It was generated as in the cases shown above by a two loop antenna driven at frequency $\omega_{ext} = 0.05$. Computational domain of size $125 \times 125 \times 500$ was discretized by $64 \times 64 \times 256$ grid and the time step was $h = 1/32$ for all cases. We used the most accurate algorithm we have for these comparison (linearly stable scheme (35) with ABM6 iterative integrator). It is seen that the error substantially depends on the amplitude of perturbations. Also while the error for low and moderate amplitude waves ($I_0 = 0.05$ and $I_0 = 0.5$) does not grow in time, a slight growth is observed for the large amplitude ($I_0 = 5$). The most striking, of course, is the difference between the CPU and GPU computations. For low amplitude waves these errors are consistent with single and double precision errors (note that there is no complete compliance of the GPU math functions with the IEEE standards for single precision), while they increase in orders of magnitude as the wave amplitude increases. It is also seen that at $t = 0$ the GPU errors are small they rapidly grow for a short time, and then stabilize. This is in contrast to the CPU computations, where the errors are almost constant in time. However, we can note that even for the worst case we have (GPU computations, $I_0 = 5$, $t = 500$), the maximum relative error achieved the value 3.6%. This level of the errors is acceptable for comparison with experiments and analysis of physical effects (there are practically no visual difference between the exact and numerical solution for plots like shown in Fig. 3).

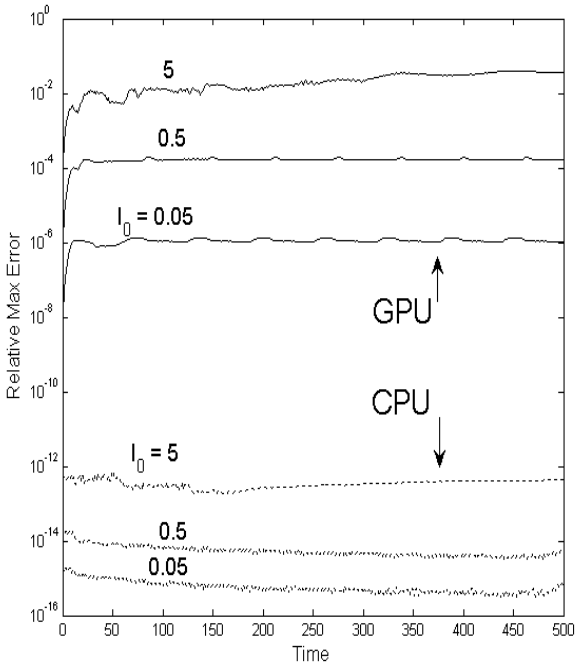

Figure 6: Maximum relative errors as functions of time for computations on CPU (double precision) and on GPU (single precision) for different wave amplitudes, chracterized by the input current I_0 shown near the curves. In all cases the integration time step $h = 1/32$ and iterative ABM6 method is used for time propagation.

5.1.5 Performance

As the most computationally expensive part of the algorithm is related to the FFTs, the algorithm complexity is scaled as $O(N_t N \log N)$, where N_t is the number of time steps, and N is the size of the problem, which is the product of three dimensions of the grid, $N = N_x N_y N_z$. In terms of the use of different time integrators the constant in this asymptotic complexity is proportional to the number of evaluations of the right hand side of the system of ODEs to be solved. The Adams-Bashforth method in this sense is the fastest, as it requires one evaluation per time step (ABM requires 2, Runge-Kutta 4th order - 4, etc.). So to compare performance of the same algorithm running on a CPU (serial code) and GPU it is sufficient to compare times per function call, or per time step for the Adams-Bashforth method.

Such a comparison is presented in Fig. 7. We used grids which sizes are powers of two and dimensions which do not differ one form the other more than 2 times, starting with $32 \times 32 \times 32$ ($N = 2^{15}$) and ending with $256 \times 256 \times 512$ ($N = 2^{25}$), which was limited by the memory size of the hardware we used (in the latter case it was 2.46 GB of the GPU global memory; the problem is scaled linearly in memory). It is seen that even a serial code has a good enough performance as it computes one step on a grid of size of order $N \sim 10^6$ for time of the order of 1 s. However the use of the GPU reduces this time approximately 10 times. It is also seen that while the CPU time is scaled approximately linearly with N (theoretically $N \log N$), the efficiency of the use of the GPU increases with the problem size. For relatively small problems ($N < 10^5$) there are no advantage in the use of the GPU. Asymptotic saturation is reached for $N \gtrsim 10^7$. So for such large N both implementations are scaled approximately linearly and the maximum ratio of the CPU and GPU times we observed is around 17.5.

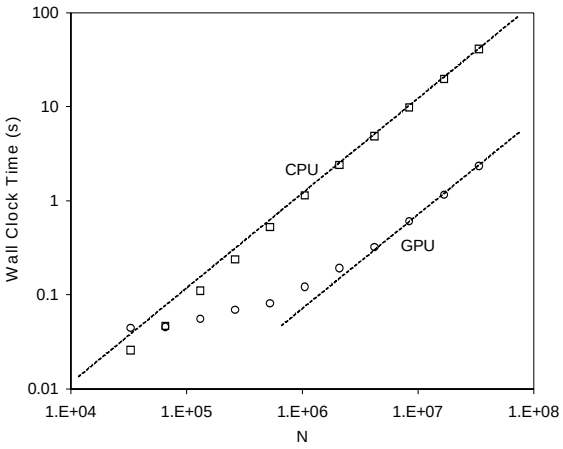

Figure 7: Comparison of the CPU and and GPU wall clock times required to perform one time step using one right-hand side evaluation per time step (e.g. the Adams-Bashforth 4th order scheme) as a function of the problem size $N = N_x N_y N_z$, where N_x, N_y, and N_z are the dimensions of the 3D grid.

6 Conclusion

The linear and nonlinear spectral and pseudospectral algorithms were used in the simulations of cold electron plasma dynamics. It is found that relatively large (nonstationary, nonlinear, 3D) problems can be efficiently computed in the personal computing environment. There are still issues in stabilization of the nonlinear codes, which are common for pseudospectral methods, and development of more stable methods, including efficient preconditioning, time splitting and implicit/semi-implicit schemes are of interest. The GPU implementations show additional substantial accelerations for many problems (10-20 times) within acceptable errors. However the use of the GPU for highly nonlinear problems can be an issue in terms of algorithm stability and performance, and additional research in this area is needed.

7 Acknowledgment

This work was supported by ONR MURI Grant 5-28828.

References

[1] H. Barkhausen, Two phenomena discovered with the aid of the new amplifier, Phys. Zeits. 20 (1919) 401-403 .

[2] N. A. Krall and A. W. Trivelpiece, Principles of Plasma Physics, McGraw-Hill, Tokyo, 1973.

[3] T. H. Stix, The Theory of Plasma Waves, AIP, New York, 1992.

[4] A. Gigliotti, W. Gekelman, P. Pribyl, S. Vincena, A. Karavaev, X. Shao, A. S. Sharma, and D. Papadopoulos, Phys. Plasmas 16(9) 092106 (2009) 1-8.

[5] A. V. Karavaev, N. A. Gumerov, K. Papadopoulos, Xi Shao, and A. S. Sharma, Generation of whistler waves by a rotating magnetic field source, Phys. Plasmas 17(1) 012102 (2010) 1-13.

[6] M. Lampe, G. Joyce, W. M. Manheimer, A. Streltsov, and G. Ganguli, Quasineutral particle simulation technique for whistlers, J. Comput. Phys. 214 (2006) 284-298.

[7] D. Shaikh, A. Das, P. K. Kaw, Hydrodynamic regime of two-dimensional electron magnetohydrodynamics, Phys. Plasmas 7(5) (2000) 1366-1373.

[8] B. Eliasson and P. K. Shukla, Dynamics of whistler spheromaks in magnetized plasmas, Phys. Rev. Lett. 99(205005) (2007) 1-4 .

[9] D. Shaikh, Theory and simulations of whistler wave propagation, J. Plasma Phys. 75 (2009) 117-132.

[10] A. S. Kingsep, K. V. Chukbar, and V. V. Yan'kov, Reviews of Plasma Physics (ed. by B. Kadomtsev), Vol. 16, p. 243, Consultants Bureau, New York, 1990.

[11] C. Canuto, M. Y. Hussaini, A. Quarteroni, and T. A. Zang, Spectral Methods in Fluid Dynamics, Springer-Verlag, Berlin Heidelberg, 1988.

[12] N. Jain and A. S. Sharma, Electron-scale structures in collisionless magnetic reconnection, Phys. Plasmas 16(5) 050704 (2009) 1-4.

[13] S. Subramaniam, A New Mesh-Free Vortex Method, Ph. D. Thesis, Florida State University, 1996.

[14] B. Fornberg and T. A. Driscoll, A fast spectral algorithm for nonlinear wave equations with linear dispersion, J. Comput. Phys.155 (1999) 456-467.

[15] S. V. Bulanov, F. Pegoraro, and A. S. Sakharov, Magnetic reconnection in electron magnetohydrodynamics, Phys. Fluids B 4(8) (1992) 2499-2508.

[16] J. P. Boyd, Chebyshev and Fourier Spectral Methods, Dover, New York, 2000.

[17] R. L. Stenzel, J. M. Urrutia, and K. D. Strohmaier, Whistler modes with wave magnetic fields exceeding the ambient field, Phys. Rev. Lett. 96(095004) (2006) 1-4.

[18] S. Chandrasekhar and P. C. Kendall, On force-free magnetic fields, Astrophys. J., 126 (1957) 457-460.

[19] J. B. Taylor, Relaxation and magnetic reconnection in plasmas, Rev. Mod. Phys. 58(3) (1986), 741-763.

8 Appendix A

For the field of a circular loop of radius a centered at the origin of the reference frame and located in the (x,y) plane we have in cylindrical coordinates $(x,y,z)=(\rho\cos\varphi,\rho\sin\varphi,z)$

$$\mathbf{l}(\mathbf{r}')=\mathbf{i}'_{\varphi},\quad dl=ad\varphi',\quad \mathbf{i}'_{\varphi}=-\mathbf{i}_x\sin\varphi'+\mathbf{i}_y\cos\varphi',\quad \mathbf{i}'_{\rho}=\mathbf{i}_x\cos\varphi'+\mathbf{i}_y\sin\varphi' \tag{49}$$

Eq. (15) yields for unit current $I_{ant}(t)=1$:

$$\mathbf{A}^*_{ant}=-\frac{4\pi a}{k^2+1}\int_0^{2\pi}\mathbf{i}'_{\varphi}e^{-i\mathbf{k}\cdot\mathbf{r}'}d\varphi'=\mathbf{i}_x\frac{4\pi a}{k^2+1}\int_0^{2\pi}\sin\varphi' e^{-i\mathbf{k}\cdot\mathbf{r}'}d\varphi'-\mathbf{i}_y\frac{4\pi a}{k^2+1}\int_0^{2\pi}\cos\varphi' e^{-i\mathbf{k}\cdot\mathbf{r}'}d\varphi'. \tag{50}$$

We have then

$$e^{-i\mathbf{k}\cdot\mathbf{r}'}=e^{-iak_\rho\cos(\varphi_k-\varphi')},\quad k_x=k_\rho\cos\varphi_k,\quad k_y=k_\rho\sin\varphi_k,\quad k_\rho=\sqrt{k_x^2+k_y^2}, \tag{51}$$

and the following expressions for components of the antenna vector potential in cylindrical coordinates

$$\begin{aligned}
&A^*_{ant,z}=\mathbf{i}_z\cdot\mathbf{A}^*_{ant}=0, \qquad (52)\\
&A^*_{ant,\rho}=A^*_{ant,x}\cos\varphi_k+A^*_{ant,y}\sin\varphi_k=\frac{4\pi a}{k^2+1}\int_{-\varphi_k}^{2\pi-\varphi_k}\sin\varphi'' e^{-iak_\rho\cos\varphi''}d\varphi''=0,\\
&A^*_{ant,\varphi}=-A^*_{ant,x}\sin\varphi_k+A^*_{ant,y}\cos\varphi_k=-\frac{4\pi a}{k^2+1}\int_{-\varphi_k}^{2\pi-\varphi_k}\cos\varphi'' e^{-iak_\rho\cos\varphi''}d\varphi''\\
&\qquad=-\frac{8\pi a}{k^2+1}\int_0^{\pi}\cos\varphi'' e^{-iak_\rho\cos\varphi''}d\varphi''=\frac{8i\pi^2 a}{k^2+1}J_1(k_\rho a),
\end{aligned}$$

where J_1 is the Bessel function of the first kind. These expressions also show that for arbitrary current $I_{ant}(t)$ we have

$$A^*_{ant,x} = -I_{ant}(t)\frac{8i\pi^2 a k_y}{k_\rho\left(k^2+1\right)}J_1\left(k_\rho a\right), \tag{53}$$
$$A^*_{ant,y} = I_{ant}(t)\frac{8i\pi^2 a k_x}{k_\rho\left(k^2+1\right)}J_1\left(k_\rho a\right).$$

Note that these expressions are not singular at $k_\rho = 0$, since $J_1\left(k_\rho a\right) = \frac{1}{2}k_\rho a + O\left(\left(k_\rho a\right)^3\right)$, $k_\rho a \ll 1$. So the asymptotic behavior of the components at low $k_\rho a$ is

$$A^*_{ant,x} \sim -I_{ant}(t)\frac{4i\pi^2 a^2 k_y}{k^2+1}\left(1+O\left(\left(k_\rho a\right)^2\right)\right), \tag{54}$$
$$A^*_{ant,y} \sim I_{ant}(t)\frac{4i\pi^2 a^2 k_x}{k^2+1}\left(1+O\left(\left(k_\rho a\right)^2\right)\right).$$